ADVANCED FUNCTIONAL MATERIALS

Supporting Information

for *Adv. Funct. Mater.,* DOI: 10.1002/adfm.202109542

Thermo-Optically Designed Scalable Photonic Films with High Thermal Conductivity for Subambient and Above-Ambient Radiative Cooling

Pengli Li, Ao Wang, Junjie Fan, Qi Kang, Pingkai Jiang, Hua Bao, and Xingyi Huang**

WILEY-VCH

Supporting Information

Thermo-Optically Designed Scalable Photonic Films for High-Performance Subambient and Above-Ambient Radiative Cooling

Pengli Li,[1] Ao Wang,[2] Junjie Fan,[2] Qi Kang,[1] Pingkai Jiang,[1] Hua Bao,[2] Xingyi Huang[1*]*

Supplementary Note 1. Optical simulation.

The discrete dipole approximation (DDA) method[1] is usually applied to determine the scattering coefficient and asymmetry factor of particles with different shapes. In this method, the particle is represented by many dipoles that interact with each other as well as the incident field. Solving the linear equations yield each dipole moment, and the radiative property can be obtained by adding the effect of all dipoles. The DDSCAT 7.3 package[2] was used to obtain the scattering cross section (C_{sca}) and asymmetry parameter (g) of a single particle surrounded by the basic media.

We considered a many-particle system in the wavelength range of 0.3–3.0 μm, and the refractive index of the basic medium was $1.45+2 \times 10^{-6}i$. Such a small absorption factor is considered but has no effect on the particle scattering field. The particle was either a sphere with a diameter of 0.393 μm and a refractive index of 2.0 or 1.6 or a disc of the same volume with a diameter-to-thickness ratio of 18:1 and a refractive index of 2.0. The volume faction of the particles was set as 40%. In the DDA method, the number of dipoles must be sufficient to make $|m|kd < 1$, where m is the refractive index, k is the wavenumber, and d is the size of each dipole. We used enough dipoles to make the calculation with $|m|kd < 0.5$, as recommended for higher accuracy.[2]

The reflectance of the photonic film was then evaluated using the Monte Carlo method with the MCML package.[3] The scattering coefficient of the system can be calculated by multiplying the particle number per volume and C_{sca}. We released 100,000 photons into the 1,000-μm-thick photonic film and finally calculated the overall reflectivity at solar wavelength (0.3–2.5 μm).

Supplementary Note 2. Thermal calculation.

In the steady-state calculation, the energy conservation equation needs to be solved. The heating power comes to the surface and the heat dissipates by convection and radiation according to the following equation:

$$P = h \cdot (T - T_{atm}) + \varepsilon \cdot \sigma \cdot (T^4 - T_{atm}^4) \quad \text{(S1)}$$

where P is the heating power, T is the surface temperature, T_{atm} is the ambient environment temperature, which is set to 27 ^{o}C, ε is the emittance, σ is the Stefan–Boltzmann constant, and h is the convective heat transfer coefficient. We used the formula given in Reference [4].

$$\overline{Nu_L} = \frac{\bar{h}L}{k} \quad \text{(S2)}$$

where the Rayleigh number,

$$Ra_L = Gr_L Pr = \frac{g\beta(T - T_{atm})L^3}{v\alpha} \quad \text{(S3)}$$

for horizontal plates,

$$\overline{Nu_L} = 0.54\, Ra_L^{1/4} \; (10^4 \lesssim Ra_L \lesssim 10^7, Pr \gtrsim 0.7) \quad \text{(S4)}$$

where Nu is the Nusselt number, L is the characteristic length of the geometry, k is thermal conductivity, Ra is the Rayleigh number, Gr is the Grashof number, Pr is the Prandtl number, g is gravitational acceleration, β is volumetric thermal expansion coefficient, v is the specific volume, α is the thermal diffusivity, $n = \frac{1}{4}$ and $\frac{1}{3}$ for laminar and turbulent flows, respectively. The temperature is linearly distributed in the film in the thickness direction so that the temperature of the heater can be obtained using the surface temperature and the thermal conductivity.

In the transient calculations, the temperature of the heater as a function of time is a one-dimensional heat conduction problem. We divided the film into 500 slices and set the time interval to be 0.5 s. At the top of the system, heat transfer should include both convection and

radiation with the same equations as in the steady-state case. We used finite-difference methods to determine the temperature as a function of time.

To further demonstrate the superior performance of the photonic films than common radiative coolers, we add calculated temperature of a simulated high performance radiative cooler. The simulated radiative cooler has a solar reflectance of 97% and thermal conductivity of 0.075 W $m^{-1}K^{-1}$. The thermal conductivity is calculated by effective medium theory and the deduced Maxwell-Eucken equation,

$$k_e = k_1 \frac{2k_1+k_2-2(k_1-k_2)v_2}{2k_1+k_2+(k_1-k_2)v_2} \quad \text{(S5)}$$

in which k_e is the thermal conductivity of the whole radiative cooler, k_1 is the thermal conductivity of the polymer, k_2 is the thermal conductivity of the scatterers, and v_2 is the volume fraction of the scatterers. Based on previous work, we assumed the radiative cooler have 60 vol% of air as scatterers here.[2]

Supplementary Note 3. Cooling power calculation.

The cooling power for subambient and above-ambient radiative cooling conditions is calculated by:

$$P_{cool}(T) = P_{rad}(T) - P_{atm}(T_{amb}) - P_{Sun} - P_{cond+conv} \quad \text{(S6)}$$

in which, the radiative power emitted by the photonic film is

$$P_{rad}(T) = A \int d\Omega \cos\theta \int_0^\infty d\lambda I_{BB}(T,\lambda)\epsilon(\lambda,\theta) \quad \text{(S7)}$$

in this equation, $\int d\Omega = 2\pi \int_0^{\pi/2} d\theta \sin\theta$ is hemisphere angular integral. $I_{BB}(T,\lambda) = \frac{2hc^2}{\lambda^5}\frac{1}{e^{hc/(\lambda k_B T)}-1}$ is the blackbody radiation spectral at temperature T, where c is the light speed, λ is the wavelength, h is Planck's constant and k_B is the Boltzmann constant.

$$P_{atm}(T_{amb}) = A \int d\Omega \cos\theta \int_0^\infty d\lambda I_{BB}(T_{amb},\lambda)\epsilon(\lambda,\theta)\epsilon_{atm}(\lambda,\theta) \quad \text{(S8)}$$

is the absorbed atmospheric thermal radiation, where $\epsilon_{atm}(\lambda,\theta) = 1 - t(\lambda)^{1/\cos\theta}$, $t(\lambda)$ is the transmittance of the atmosphere in the zenith direction.

$$P_{Sun} = A \int_0^\infty d\lambda \epsilon(\lambda,\theta_{Sun}) I_{AM1.5}(\lambda) \quad \text{(S9)}$$

is the absorbed solar heat.

$$P_{cond+conv}(T,T_{amb}) = Ah_c(T_{amb} - T) \quad \text{(S10)}$$

is the non-radiative power lost. $h_c = h_{cond} + h_{conv}$ is the non-radiative heat coefficient composed of conductive and convective heat generation.

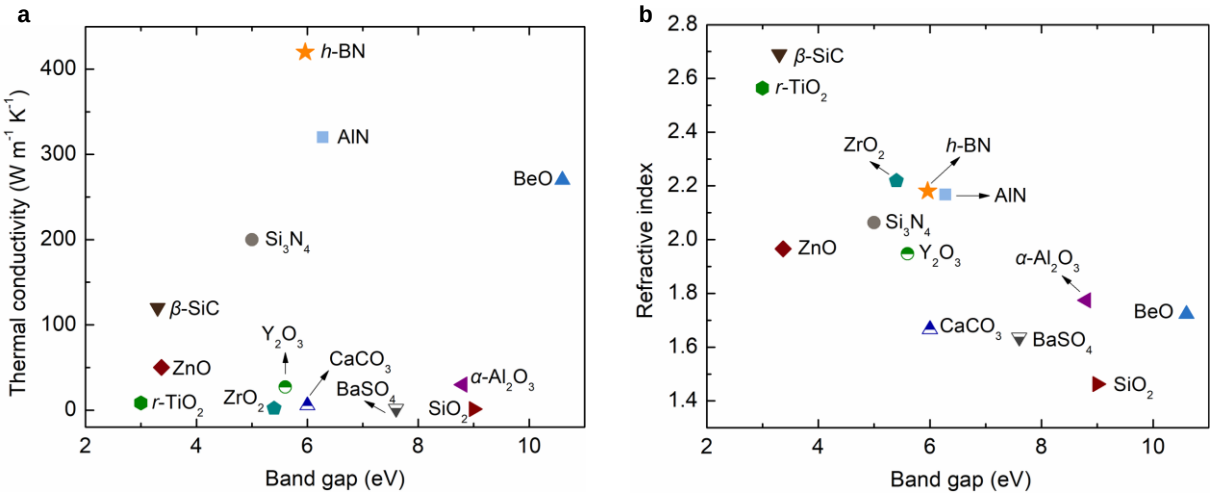

Figure S1. Thermal conductivity (a), refractive index (b) over band gap of commonly used dielectric particle with high refractive index or high thermal conductivity. Reference: *h*-BN [5], AlN [6], BeO [7], Si_3N_4 [7a, 8], *β*-SiC [7a, 9], ZnO [10], *r*-TiO_2 [11], ZrO_2 [12], $CaCO_3$ [12c, 13], $BaSO_4$ [14], *α*-Al_2O_3 [7a, 15], SiO_2 [16], Y_2O_3 [17].

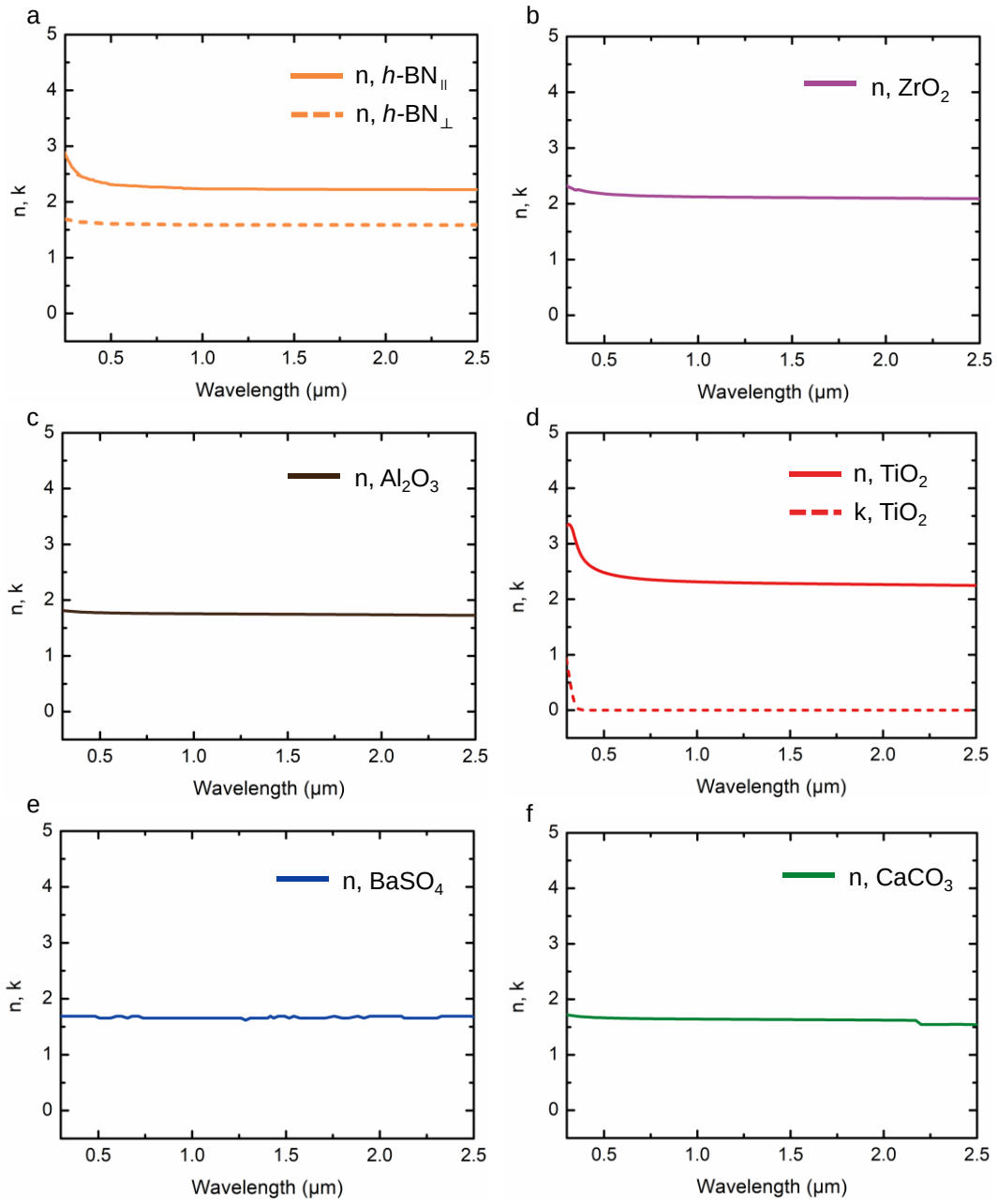

Figure S2. Refractive index and extinction coefficient of *h*-BN (a) and commonly used materials, b) ZrO_2, c) Al_2O_3, d) TiO_2, e) $BaSO_4$, f) $CaCO_3$.

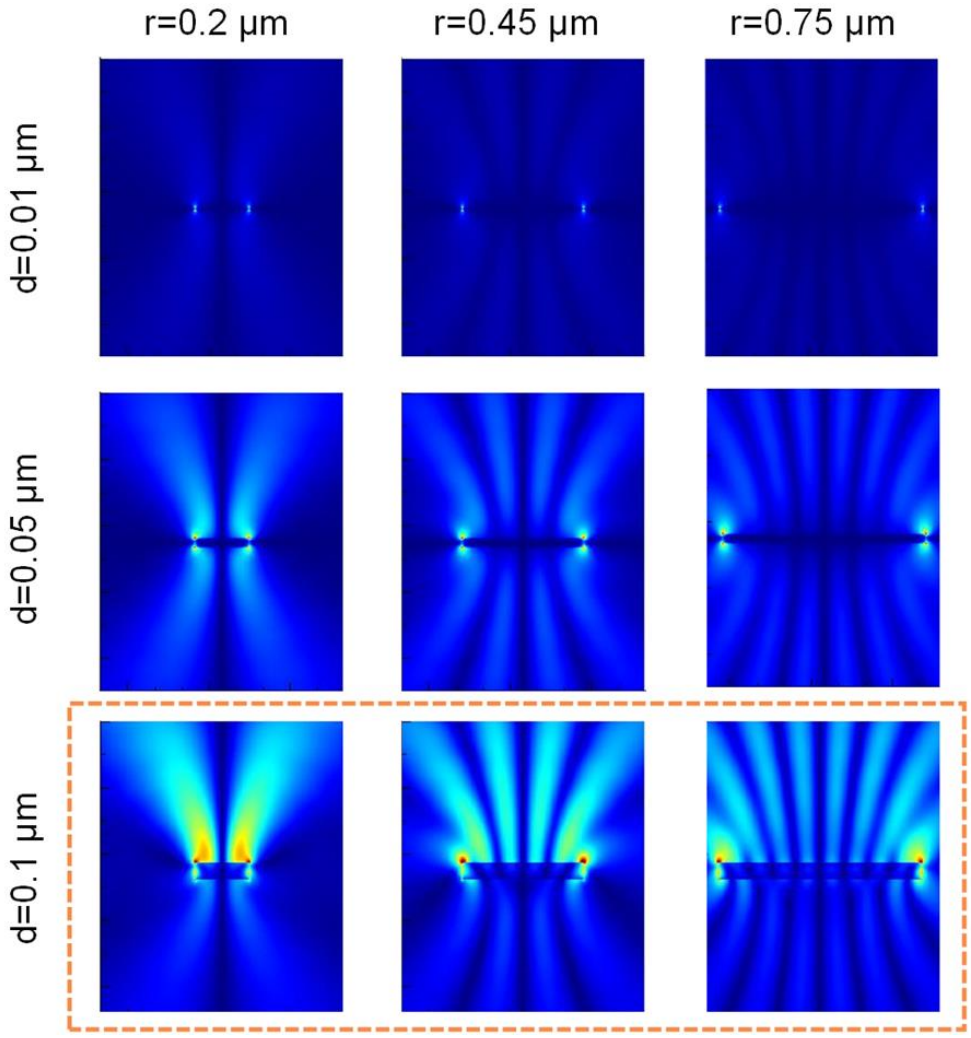

Figure S3. FDTD simulation of a 2D particle with different size (thickness: d, radius: r), illuminated at 0.4-μm wavelength upward. It can be observed that the directivity of scattering is mainly influenced by the thickness of the plate. When the thickness of the plate (0.1 μm) is closed to light wavelength, the plate shows obvious forward scattering, which is like Mie scattering. On the contrary, the plate presents isotropic scattering when its thickness is much smaller than the light wavelength.

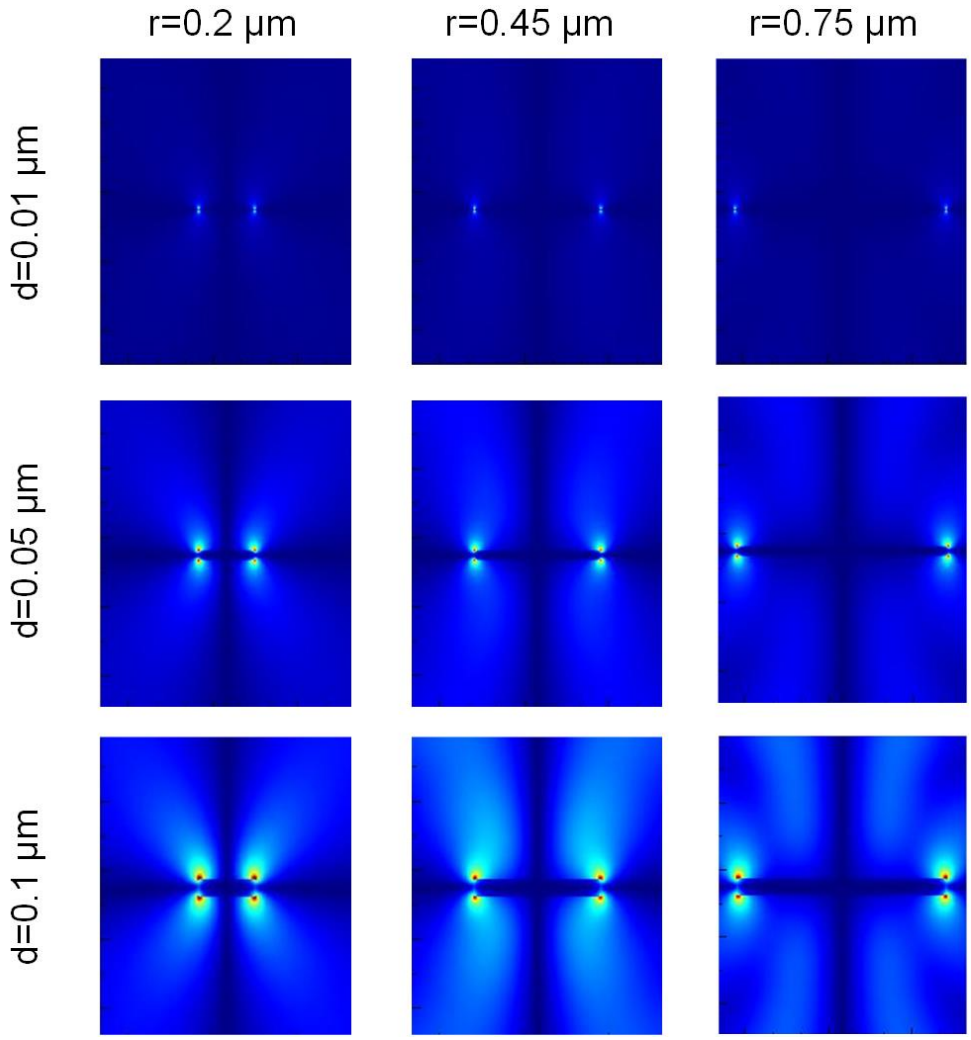

Figure S4. FDTD simulation of a 2D particle with different size (thickness: d, radius: r), illuminated at 1-μm wavelength upward. The light wavelength is much larger than the thickness of the plates, so they all mainly present isotropic scattering.

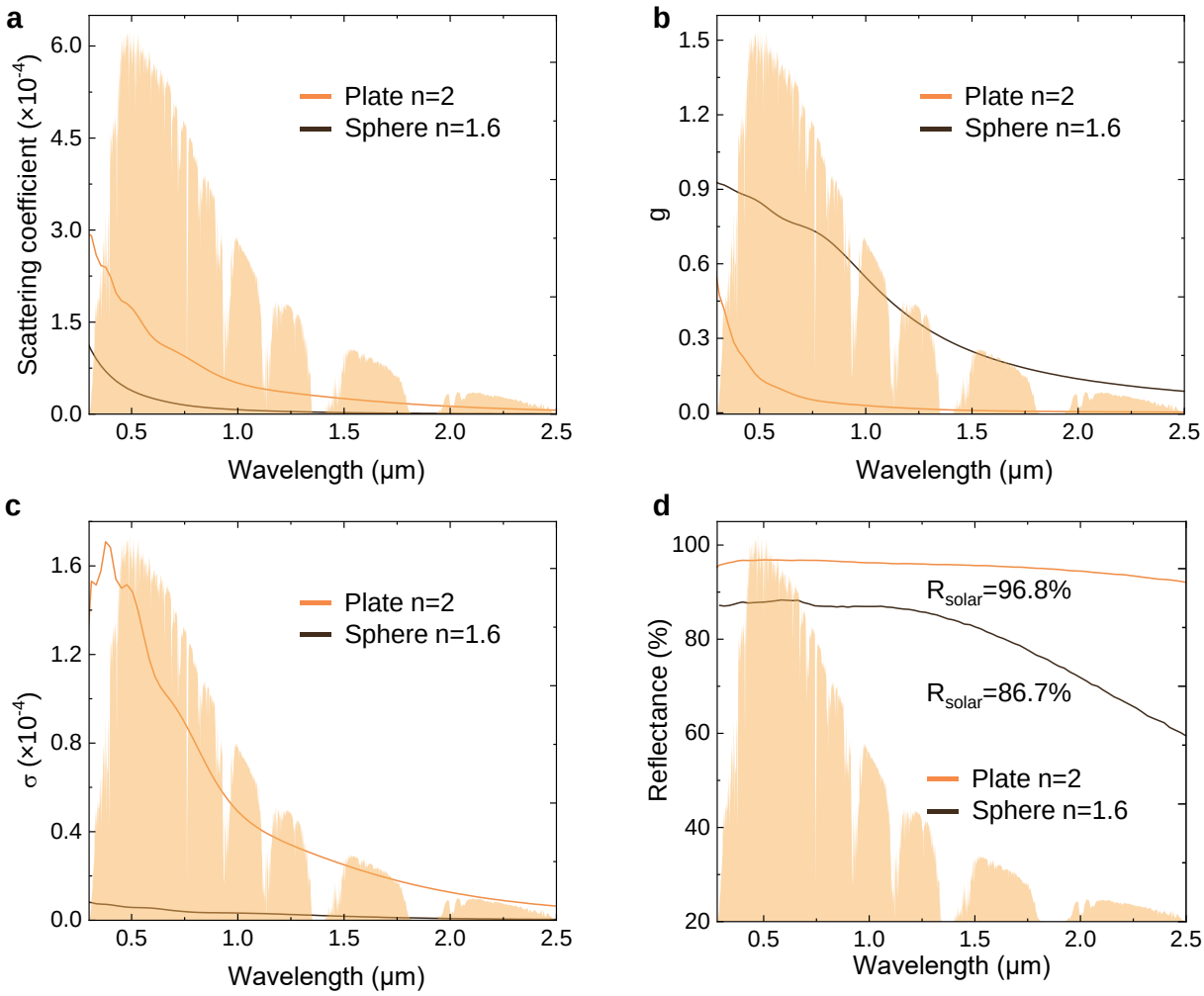

Figure S5. Optical simulations of 2D and spheric particles with different refractive index. a) Scattering coefficient of a plate (diameter = 0.9 μm, thickness = 0.05 μm, and refractive index = 2) and a sphere (of the volume as the plate, with diameter = 0.39 μm and refractive index = 1.6). b) Light scattering asymmetry factor (g) of the plate and sphere in (a). c) Angle-weighted scattering coefficient (σ) of the plate and sphere in (a). d) Simulated reflectance of 40 vol% loaded photonic structures at a thickness of 1 mm.

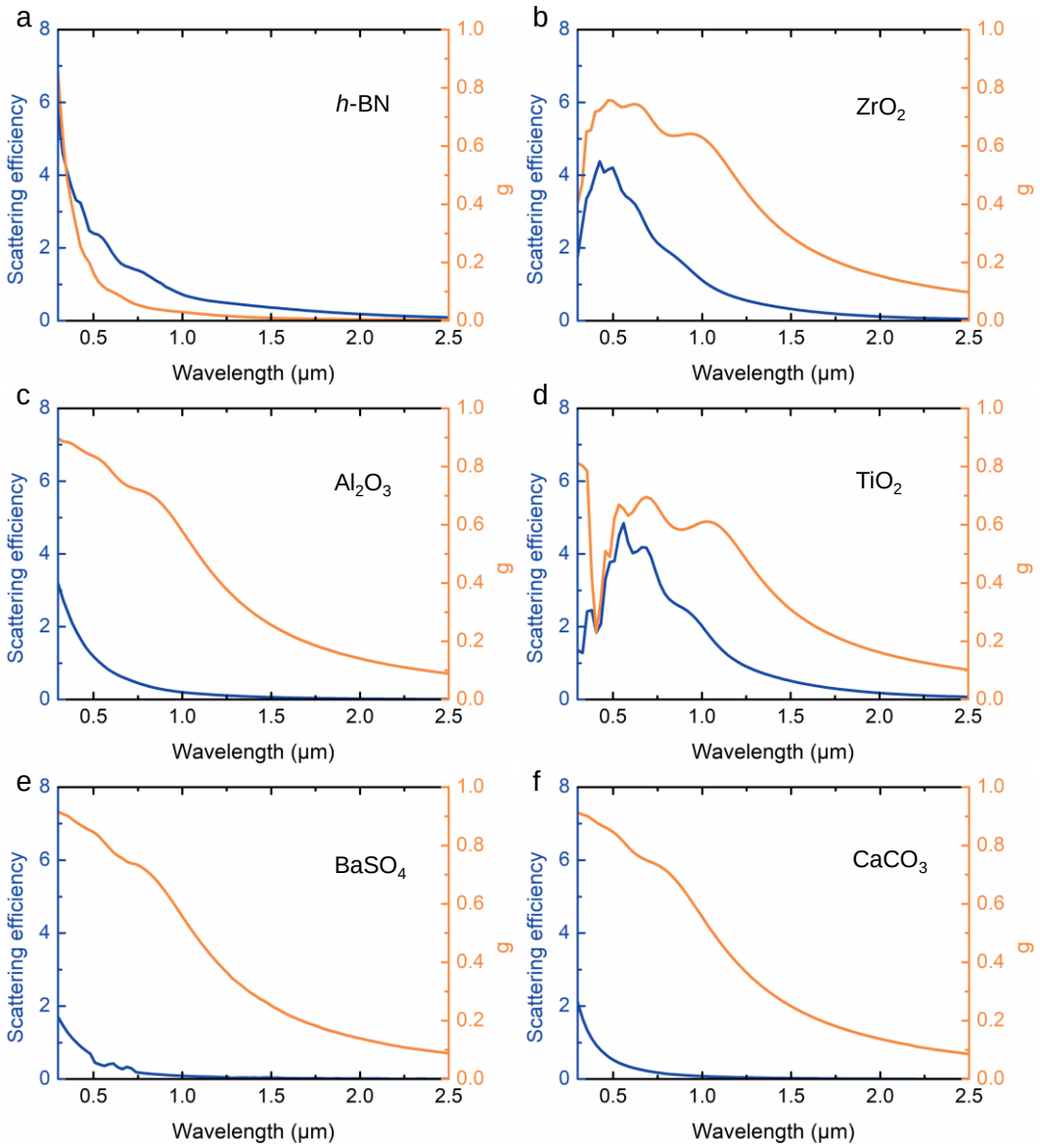

Figure S6. Scattering efficiency and asymmetry factor of *h*-BN (a) and commonly used materials, b) ZrO_2, c) Al_2O_3, d) TiO_2, e) $BaSO_4$, f) $CaCO_3$.

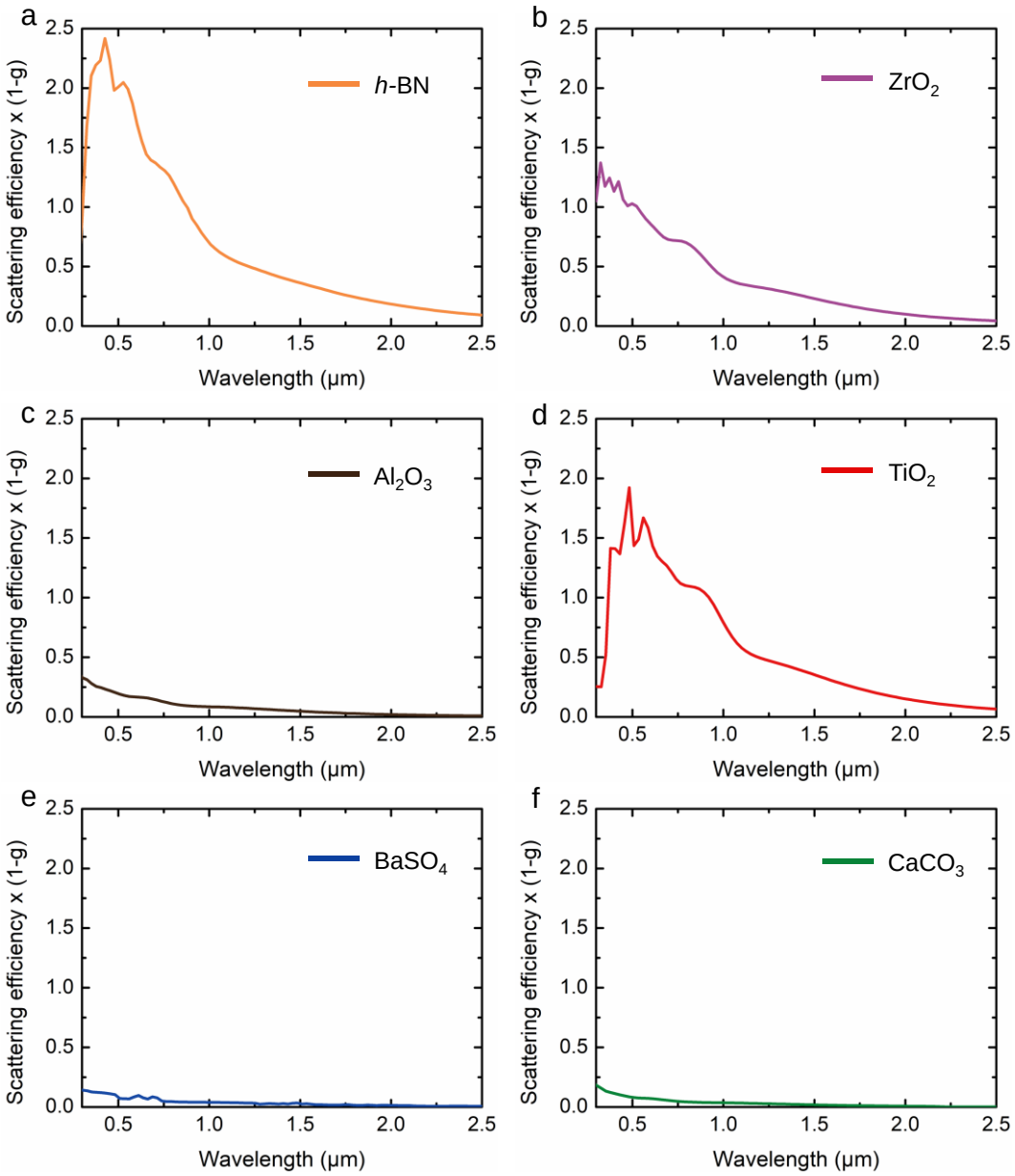

Figure S7. Angle-weighted scattering efficiency of *h*-BN (a) and commonly used materials, b) ZrO_2, c) Al_2O_3, d) TiO_2, e) $BaSO_4$, f) $CaCO_3$.

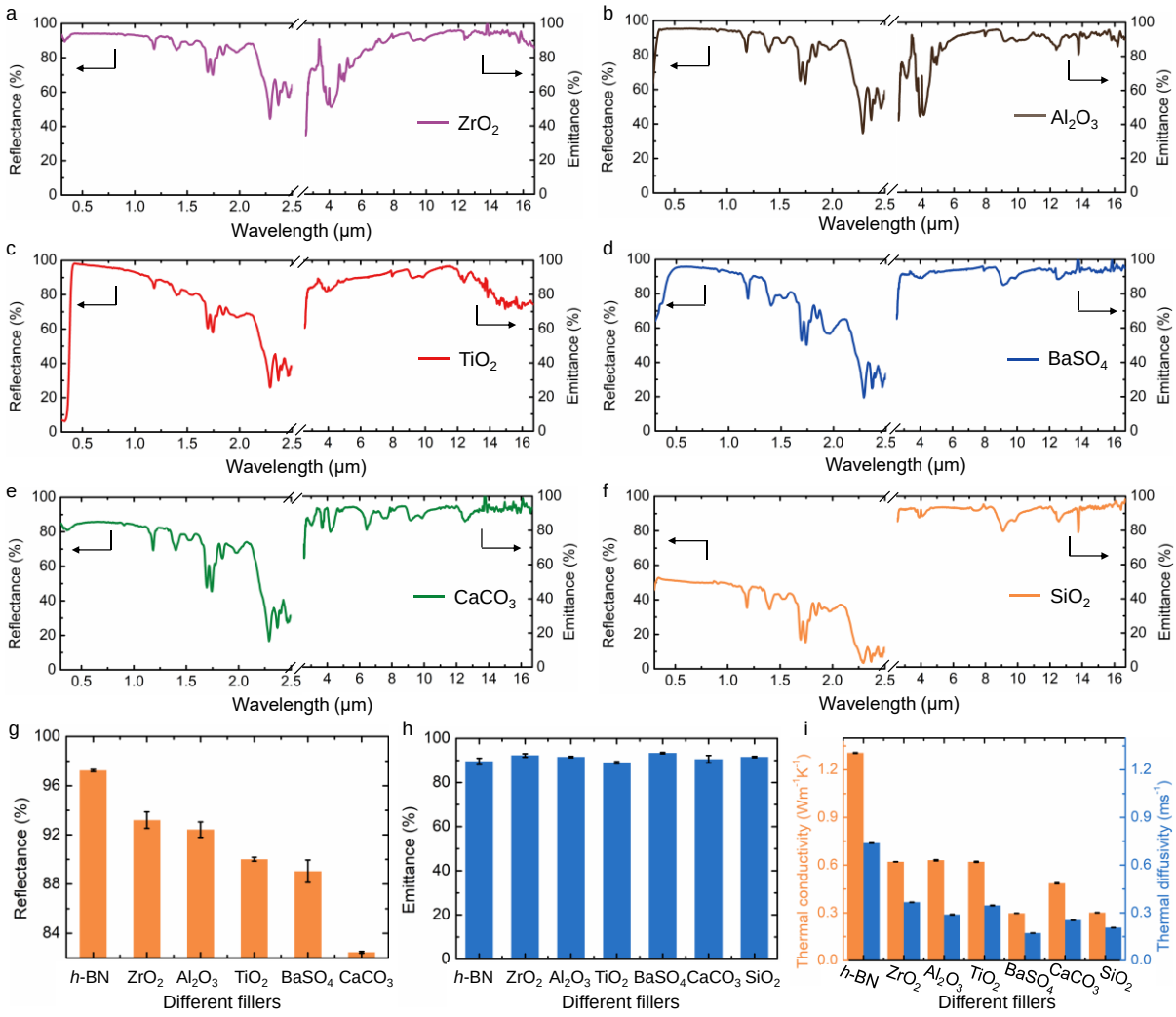

Figure S8. Reflectance and emittance of PDMS based photonic films (1,000 μm thick) filled with different scatterers (40.5 vol%) at UV-VIS-IR wavelength, a) ZrO_2, b) Al_2O_3, c) TiO_2, d) $BaSO_4$, e) $CaCO_3$, f) SiO_2. Solar reflectance (g), infrared emittance (h) and thermal conductivity/diffusivity (i) of PDMS based photonic films filled with different scatterers.

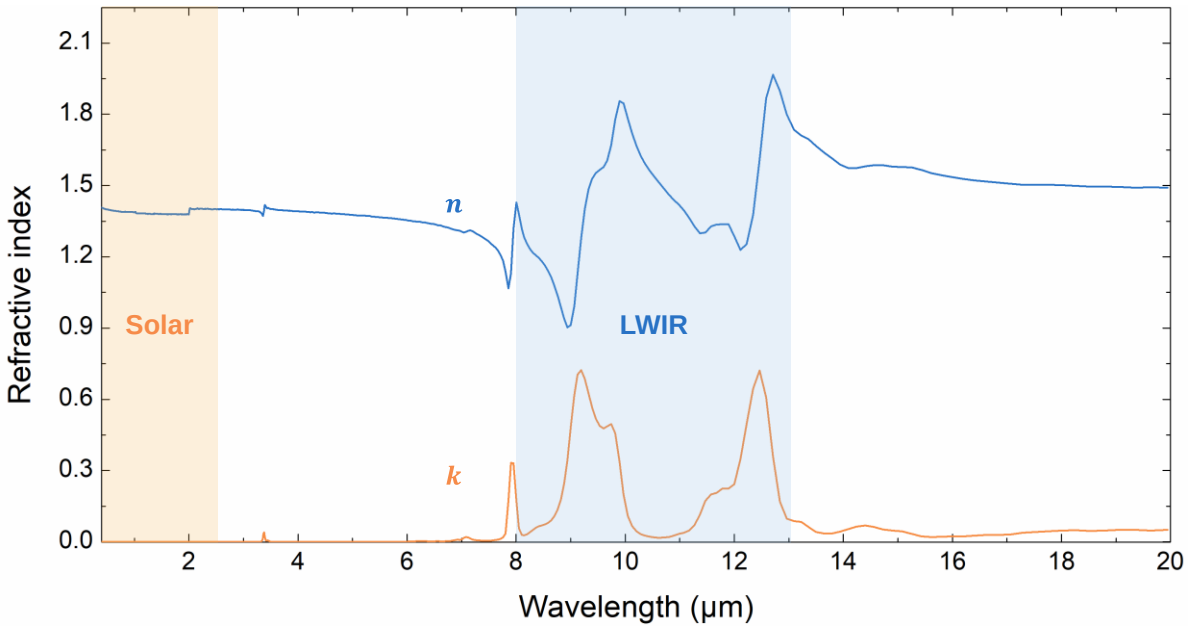

Figure S9. Refractive index (n) and extinction coefficient (k) of PDMS at different wavelength[18]. It can be observed that PDMS has low extinction coefficient in the solar spectrum but has five main extinction coefficient peaks in the 8-13 μm atmosphere's long-wave infrared (LWIR) transmission window.

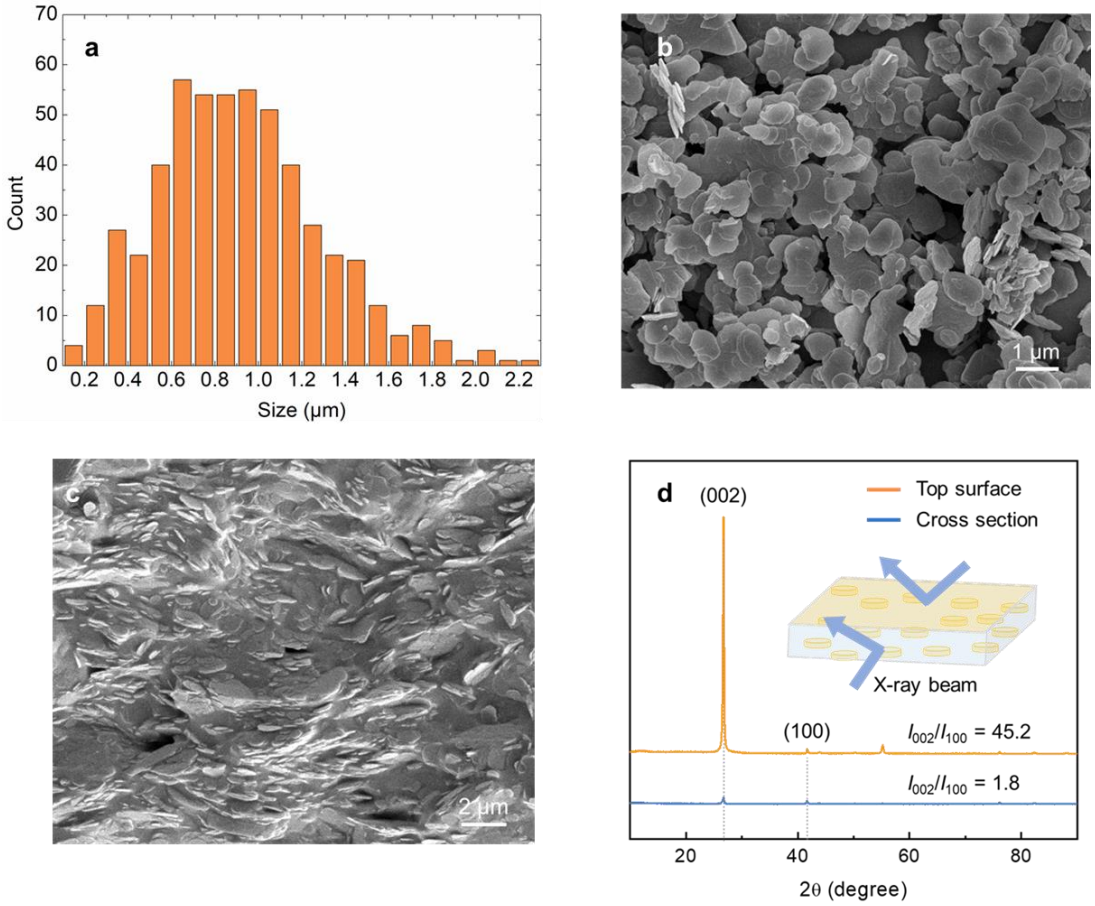

Figure S10. Distribution of the *h*-BN nanoplates in the PDMS matrix. a) Diameter distribution of the *h*-BN nanoplate. b) SEM image of *h*-BN nanoplate. c) Fracture surface SEM image of the photonic film. d) XRD patterns of the photonic film at different direction.

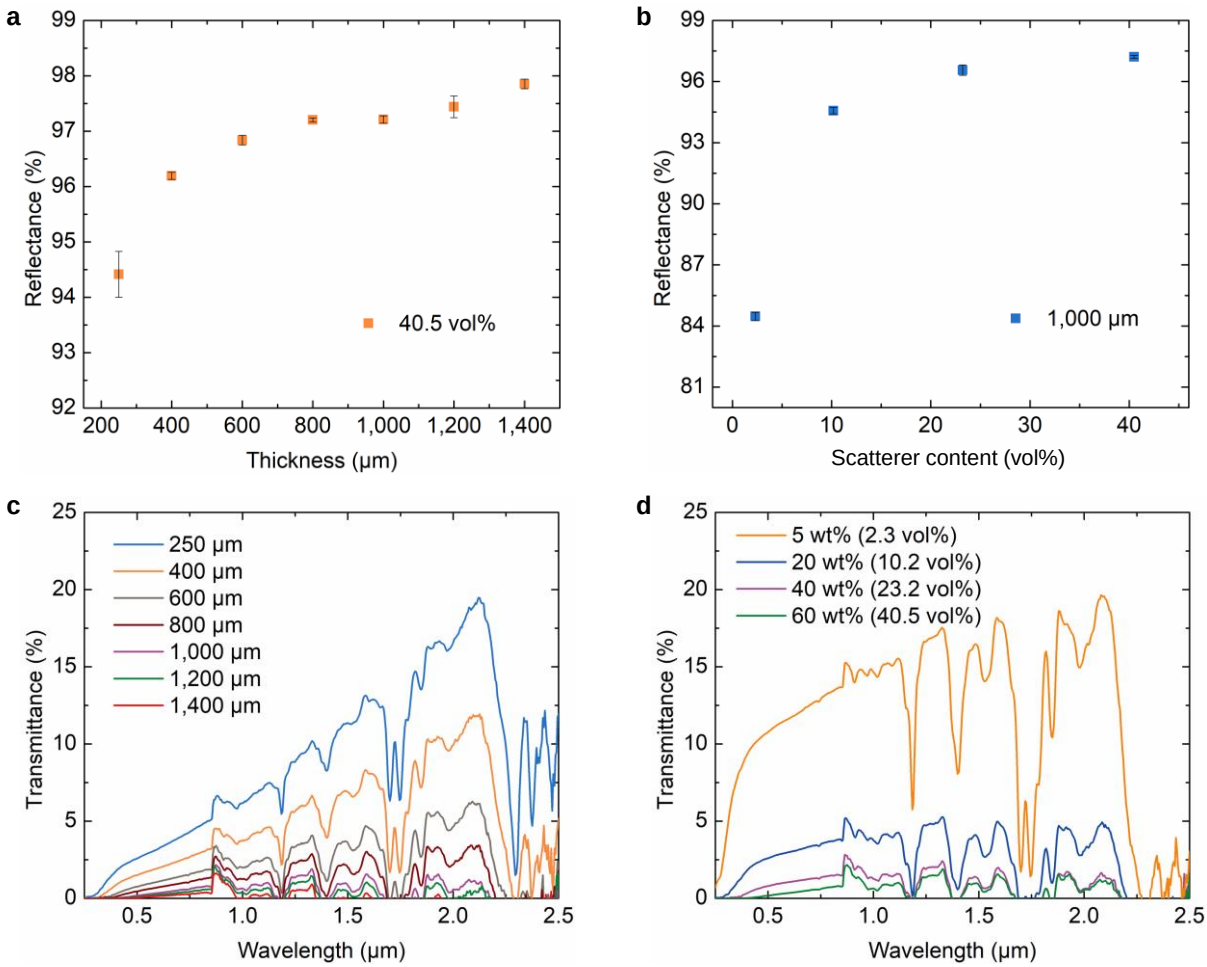

Figure S11. Influence of thickness and scatterer content over the optical properties at solar wavelengths. a) Solar reflectance of the photonic films over different thickness at scatterer content of 40.5 vol%. b) Solar reflectance of the 1,000 μm thick photonic films over different scatterer content. c) Transmittance spectrum of the photonic films over different thickness at scatterer content of 40.5 vol%. d) Transmittance spectrum of 1,000 μm thick photonic films over different scatterer content. The error bars represent the standard deviation over three different samples.

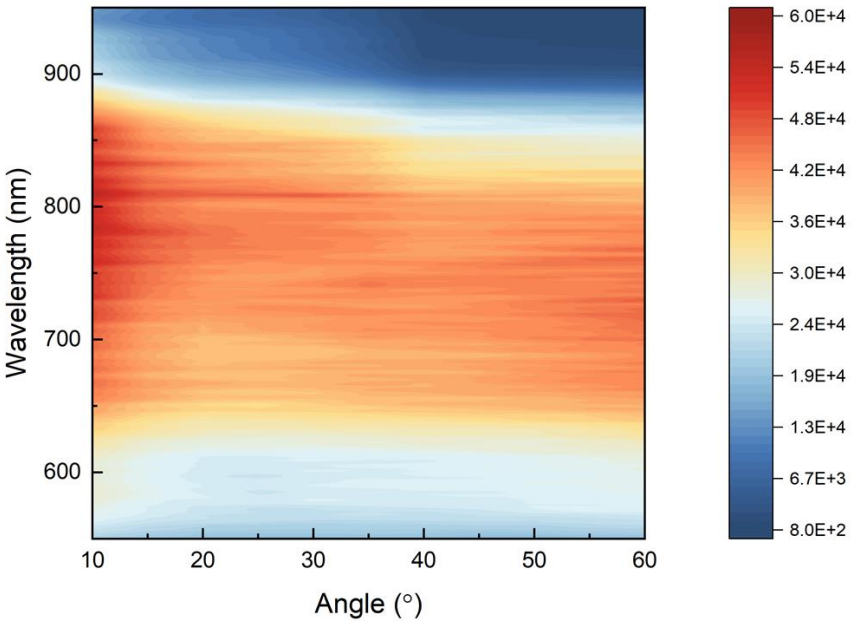

Figure S12. Full angle reflection results of the photonic films.

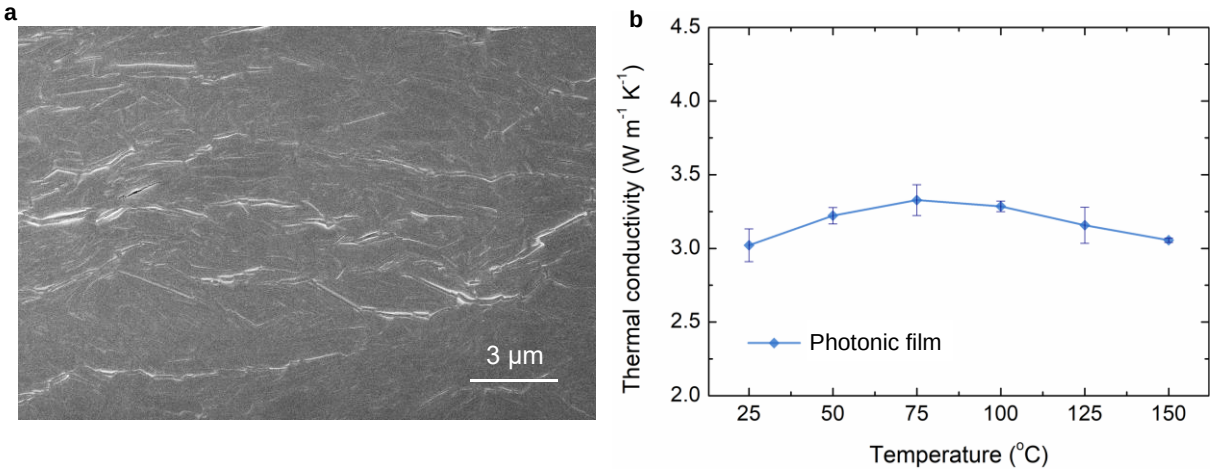

Figure S13. Thermally conductive pathways of *h*-BN formed in the photonic film. a) SEM image of the polished cross-section of photonic film. b) Thermal conductivity of the photonic film along the in-plane direction. The error bars represent the standard deviation over three independent measurements at different regions of the samples.

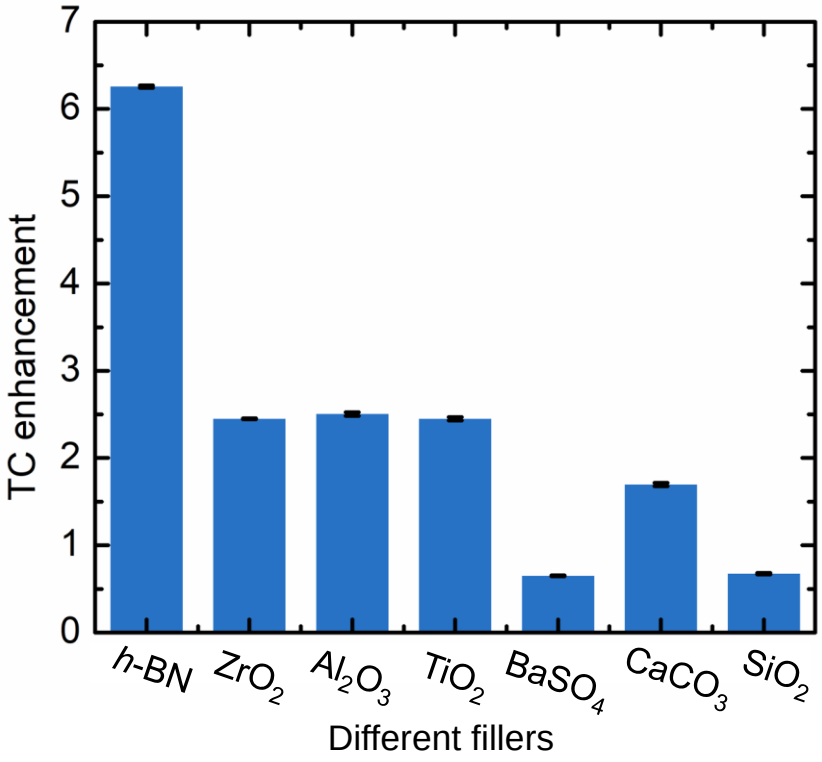

Figure S14. Thermal conductivity enhancement of the photonic films filled with different particles.

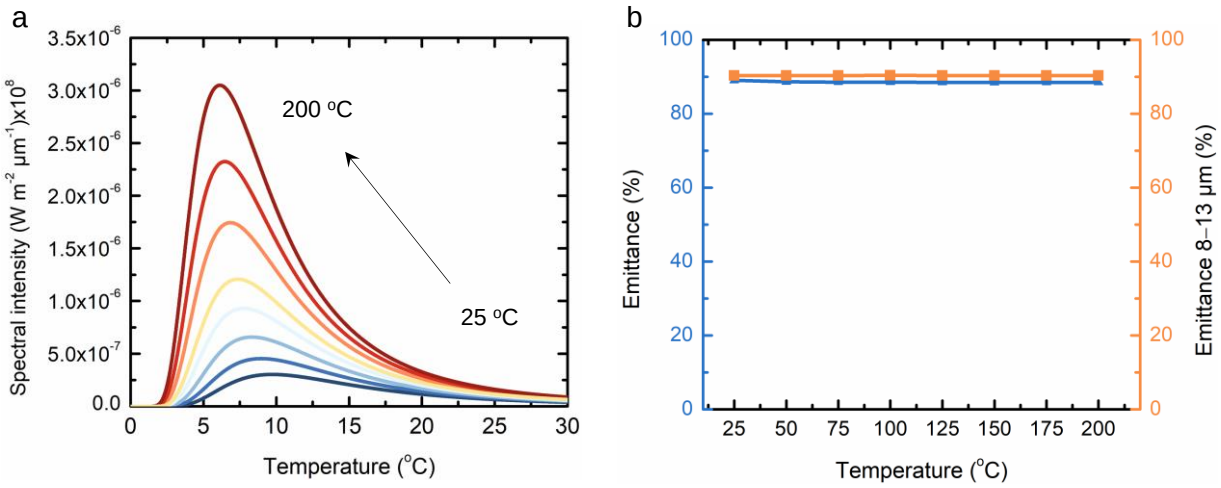

Figure S15. a) Blackbody remittance spectra at different temperatures. b) Calculated IR emittance and emittance between 8–13 μm of the photonic film as a function of temperature.

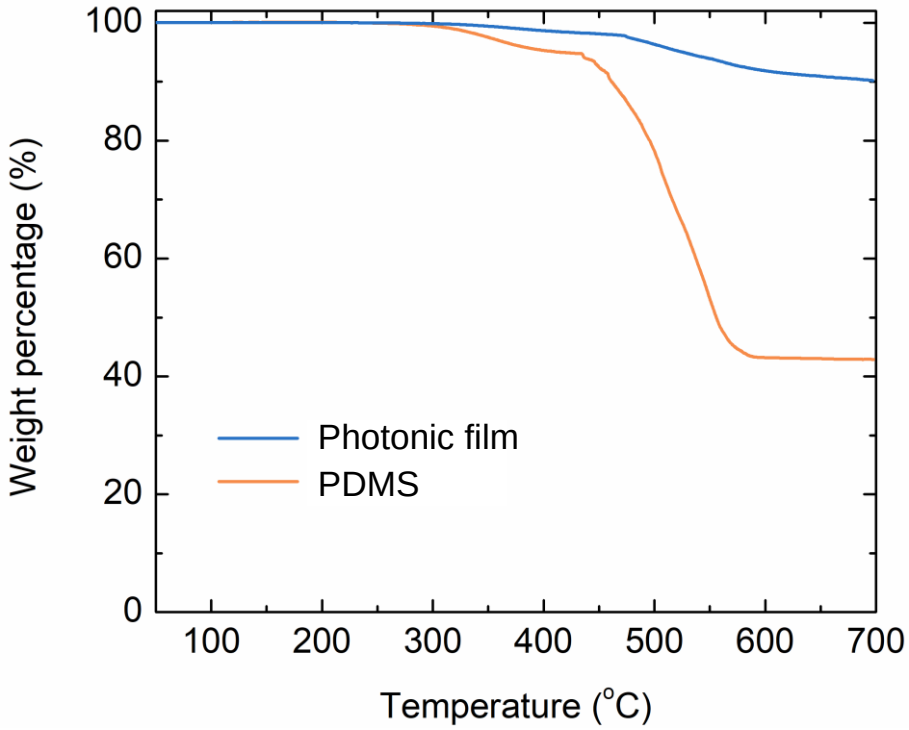

Figure S16. Weight loss of photonic film and PDMS at different temperatures during air atmosphere. In the composite, the weight percentage of *h*-BN nanoplate is 60% (40.5 vol%). However, the residual weight of the photonic film at 700 °C is much larger than the theoretical value considering the residual weight of pure PDMS. This may ascribe to the gas barrier property of *h*-BN nanoplate in the photonic film that block the permeation of oxygen. Therefore, the oxidative decomposition process is slowed down.

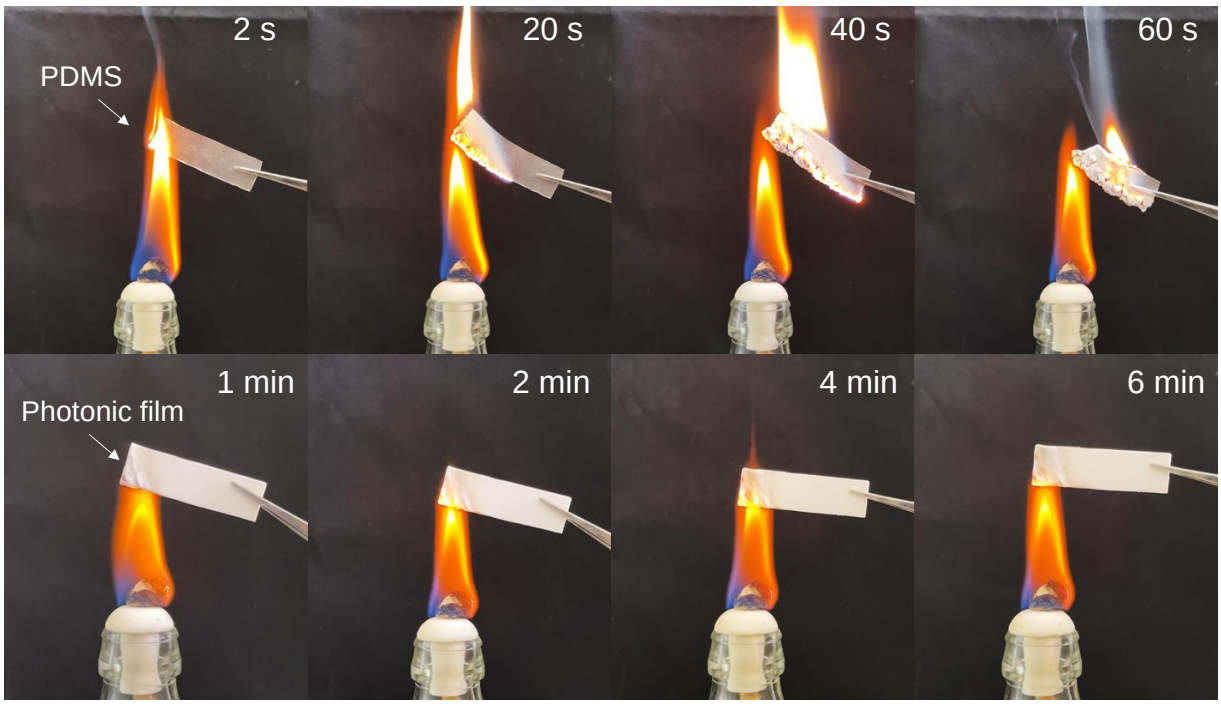

Figure S17. Flame resistance of PDMS and photonic film. The photonic film exhibits excellent self-extinguished property compared to the PDMS matrix.

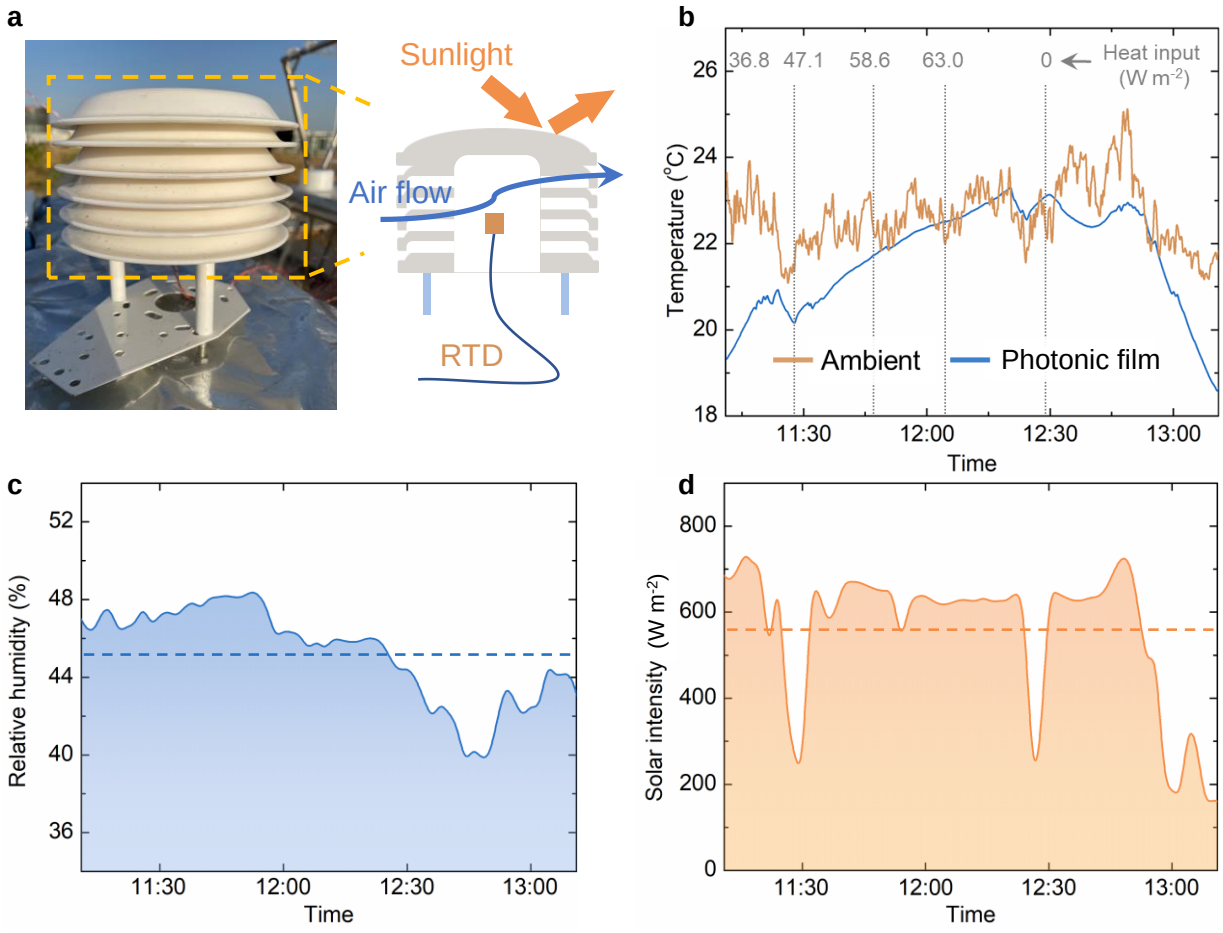

Figure S18. Outdoor sub-ambient radiative cooling power test. a) Photograph and schematic illustration of the Stevenson screen we used when measured the ambient temperature. b) Temperature of ambient and photonic film, in response to step-wise increasing heat input. When the temperature of photonic film catches up to that of ambient, the radiative cooling power is equal to the input heat power. c) and d) Relative humidity (c) and solar intensity (d) during the subambient radiative cooling power measurement period. The dotted line represents the average value during the measurement period.

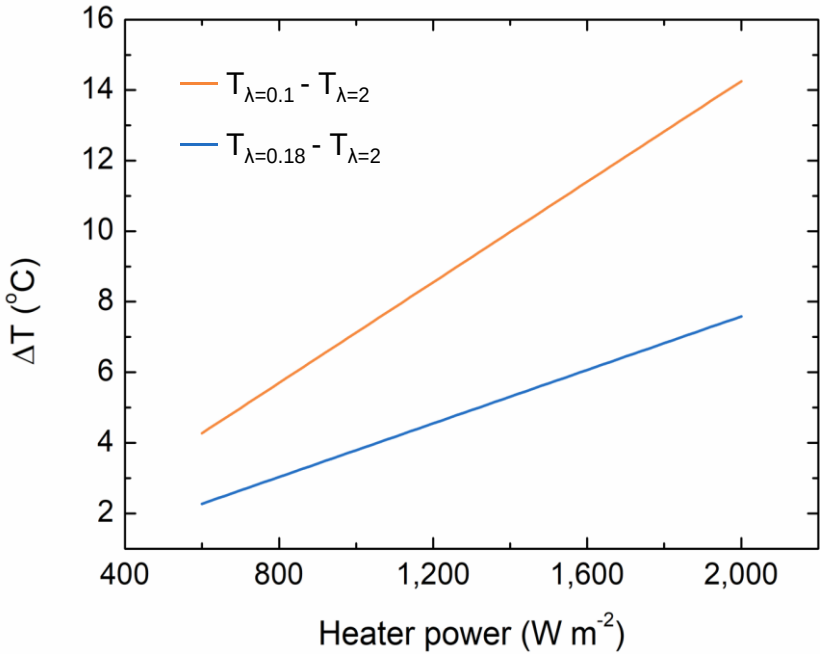

Figure S19. Temperature difference of the heater covered by different photonic films at the function of the heater power. Thickness and infrared emittance of the film covering the heater were fixed at 1 mm and 0.9, respectively. The role of thermal resistance on heat dissipation becomes more prominent as the heat flux increases.

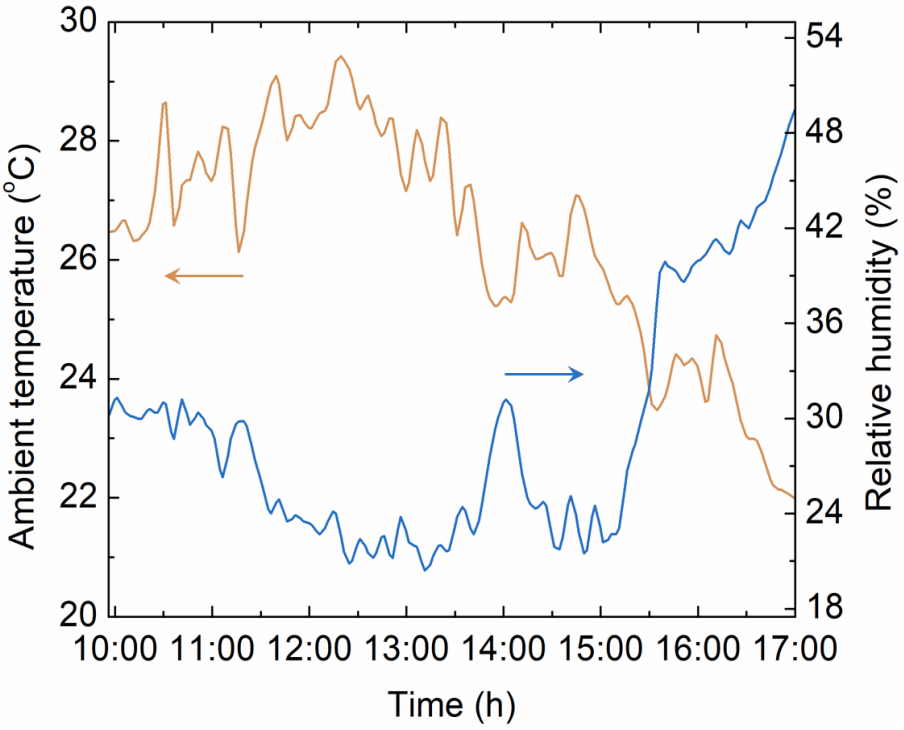

Figure S20. Real-time recorded ambient temperature and relative humidity during the outdoor above-ambient radiative cooling test.

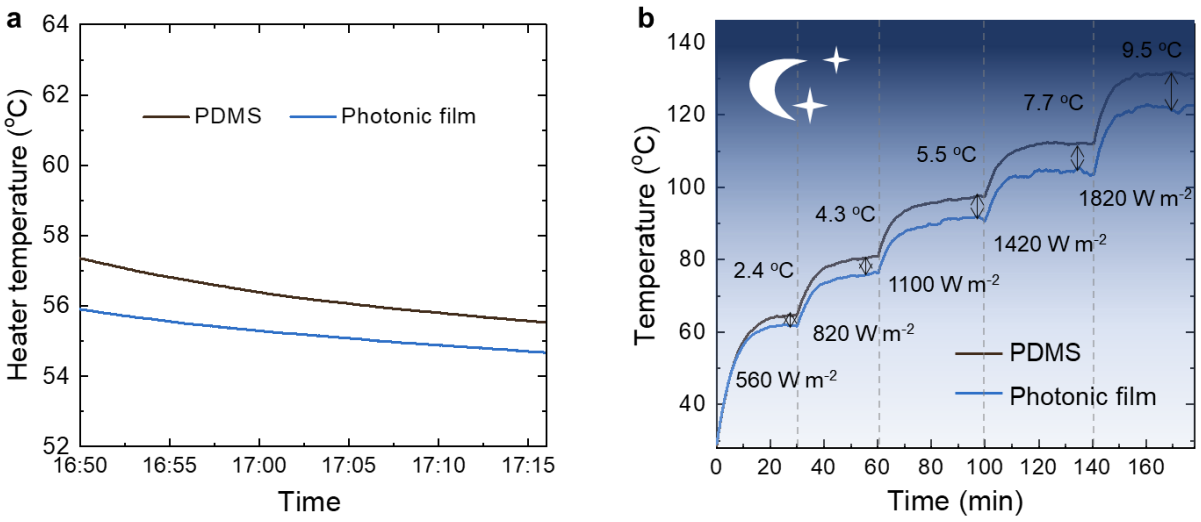

Figure S21. a) Temperature of PDMS and Photonic film after sunset. b) Temperature of PDMS and Photonic film with different heat flux after sunset.

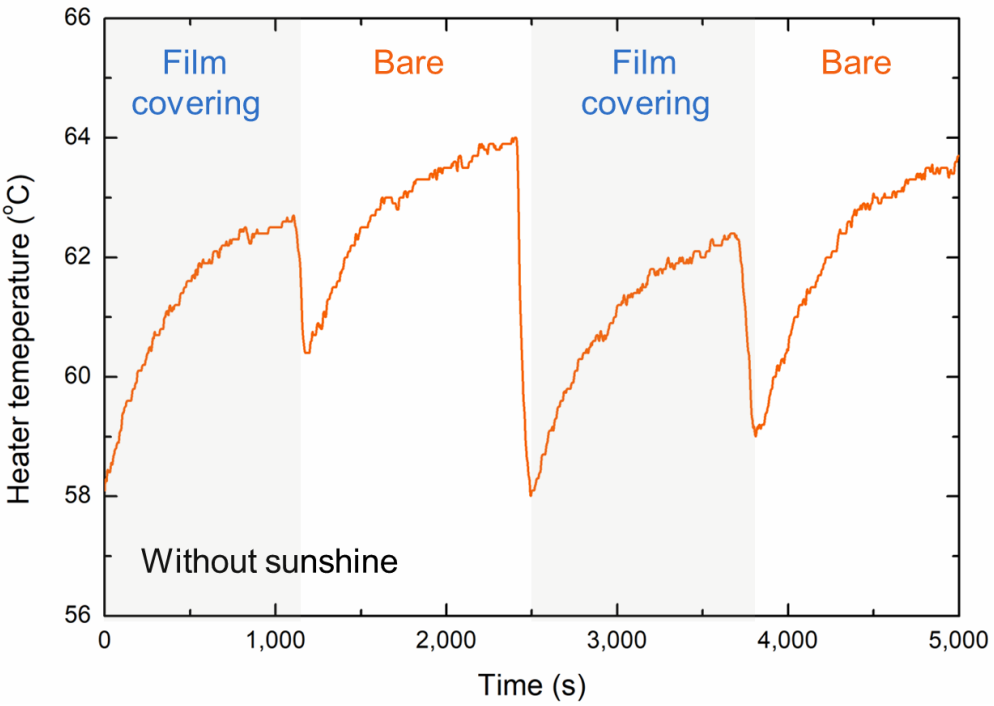

Figure S22. Temperature of the heater inside the AAO box with and without the photonic film covering. The test is completed in the environment without solar intensity to exclude the influence of solar reflectance.

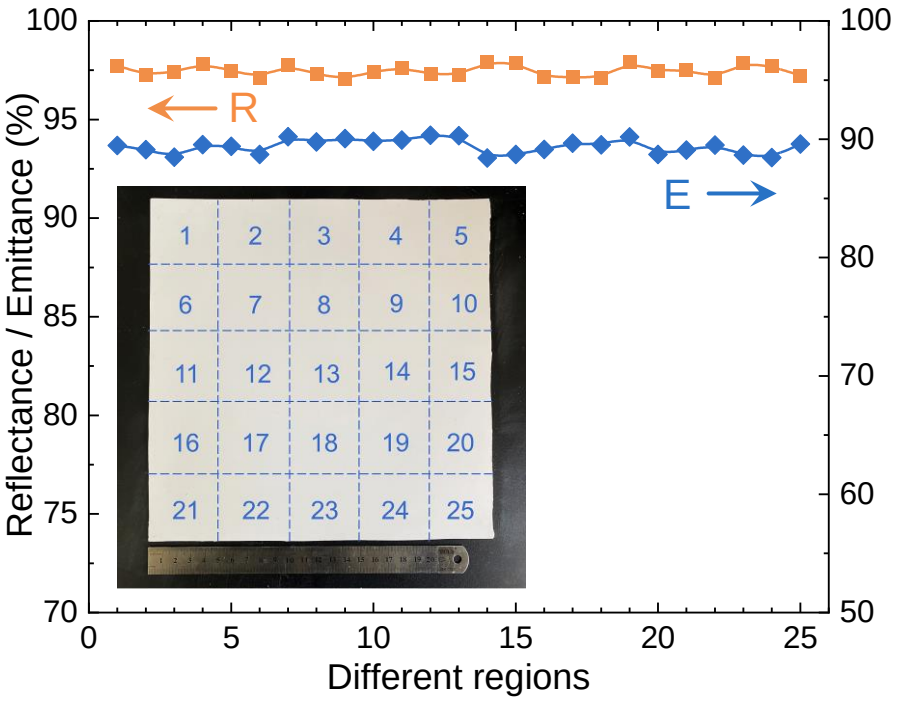

Figure S23. Characteristic reflectance and emittance tested at different regions of the 25 × 25 cm^2 area of the 1.4-mm-thick photonic film.

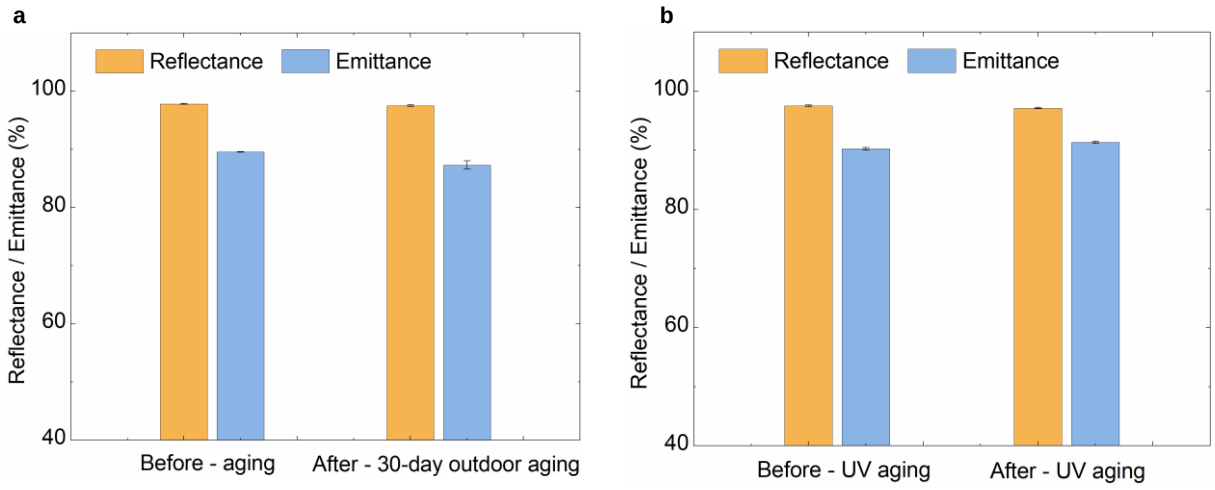

Figure S24. a) Reflectance and emittance of photonic film before and after the 30-day outdoor ageing test. b) Reflectance and emittance of photonic film before and after 72-hour UV accelerated ageing test. Each UV accelerated ageing cycle has three stages, 8 hours under 0.76 ± 0.02 W m^{-2}×nm UVA-340 light with blackboard temperature of 50 ± 3 ^{o}C, 0.25 hours of water spraying, 3.75 hours of condensation with blackboard temperature of 50 ± 3 ^{o}C. The error bars represent the standard deviation over three different samples.

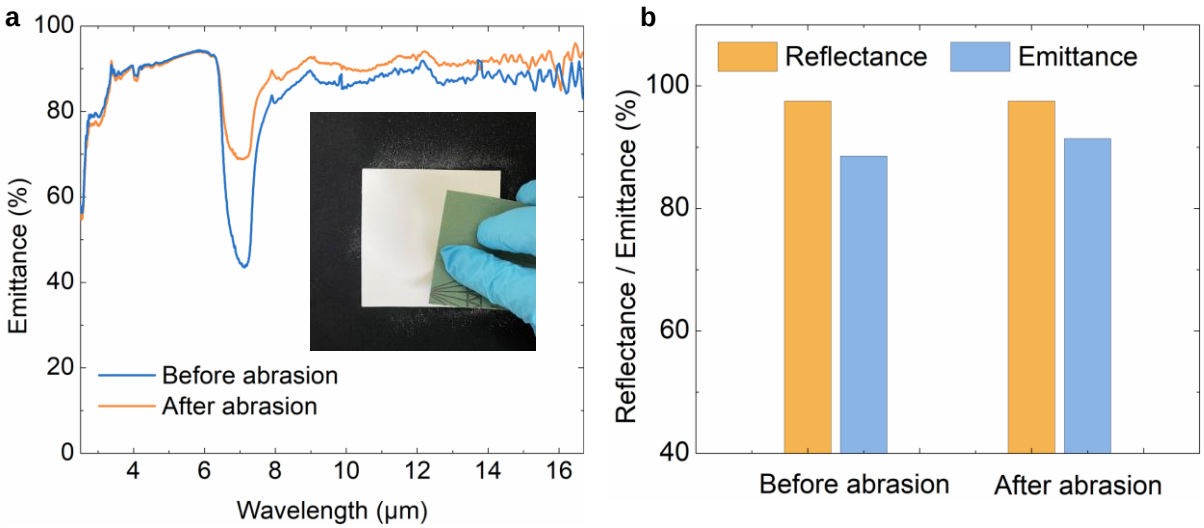

Figure S25. Optical property of the photonic film before and after abrasion. a) Infrared emittance spectrum of the photonic film before and after abrasion. The inset is the sample after abrasion. b) Solar reflectance and infrared emittance among 8–13 μm of the photonic film before and after abrasion.

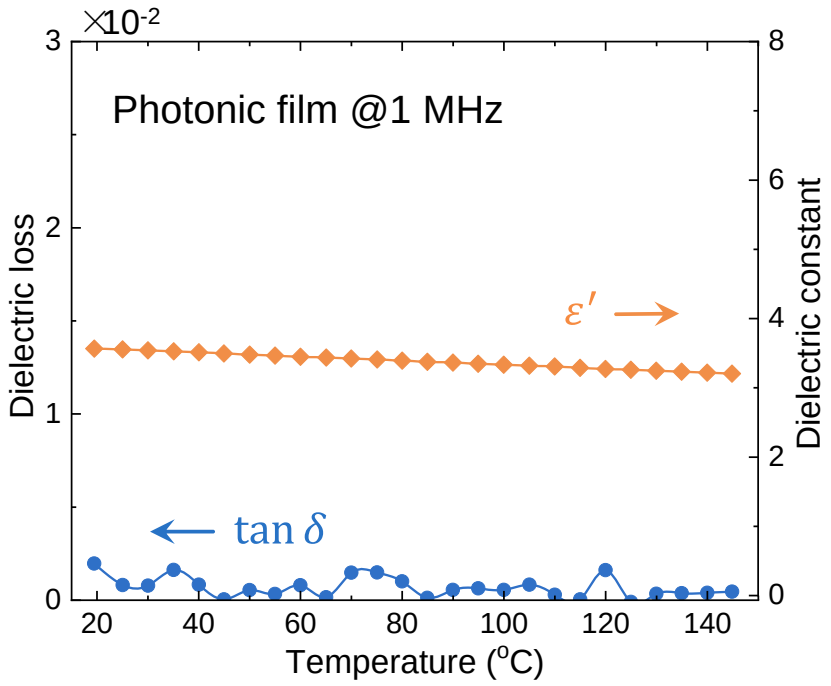

Figure S26. Temperature-dependent dielectric constant and dielectric loss of the photonic film at 1 MHz frequency.

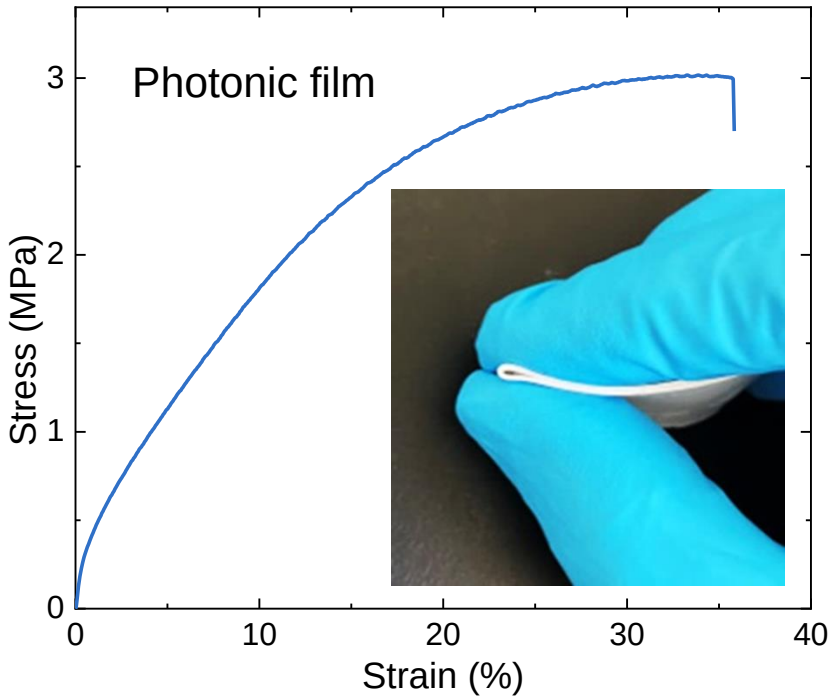

Figure S27. Stress–strain curve of photonic film. The inset shows the bent photonic film. The error bars represent the standard deviation over three different samples.

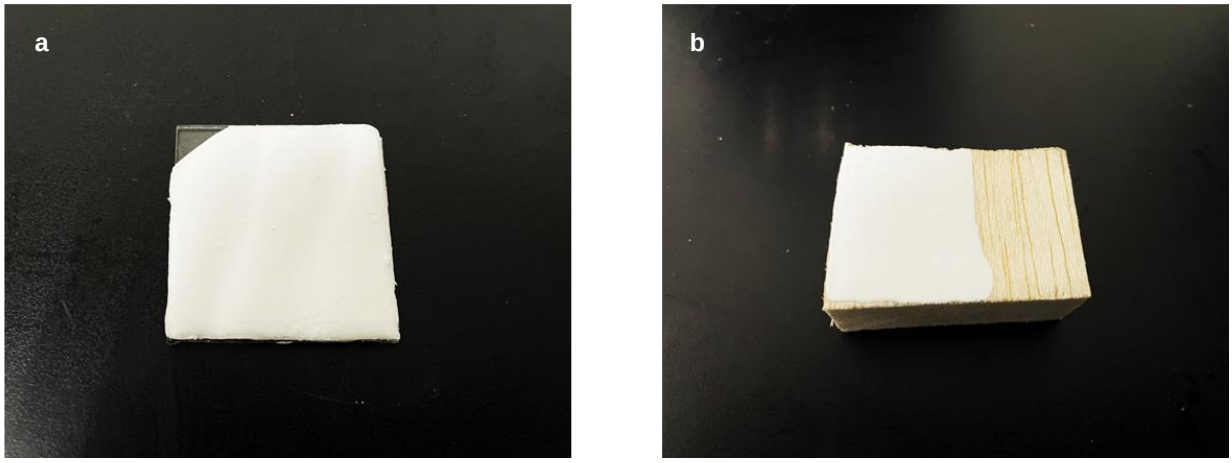

Figure S28. Optical photographs of PVDF-HFP/*h*-BN photonic paint coated glass (a) and wood (b). The photonic paint was made by mixing PVDF-HFP and *h*-BN with acetone solvent.

Table S1. Comparison of solar reflectance of the radiative coolers.

Materials	Scatterer	Solar reflectance	Thickness (μm)	Scatterer content	Thermal resistance
PVDF-HFP / TiO_2[19]	TiO_2	0.925	1,000	93 wt% / 85 vol%	Large
PVDF-HFP / Al_2O_3[19]	Al_2O_3	0.945	1,000	96 wt% / 93 vol%	Large
PVDF-HFP / $BaSO_4$[19]	$BaSO_4$	0.98	1,000	94 wt% / 86 vol%	Large
PVDF-HFP / PTFE[19]	PTFE	0.94	1,000	80 wt% / 77 vol%	Large
Porous PVDF-HFP[20]	Air	0.98	960	42 wt% / 50 vol%	Very large
Acrylic-$CaCO_3$	$CaCO_3$	0.955	400	80 wt%/ 60 vol%	Large
PDMS / Al_2O_3 with photonic structure[21]	Al_2O_3	0.95	500	50 wt% / 22 vol%	Large
Wood[22]	Air	0.96	2,000	/	Very large
This work	***h*-BN**	**0.973**	**1,000**	**60 wt% / 41 vol%**	**Very low**
This work	***h*-BN**	**0.98**	**1,400**	**60 wt% / 41 vol%**	**Very low**
This work	***h*-BN**	**0.965**	**1,000**	**40 wt% / 23 vol%**	**Very low**

References:

[1] B. T. Draine, P. J. Flatau, *J. Opt. Soc. Am. A* **1994**, 11, 1491.

[2] B. T. Draine, P. J. Flatau, *arXiv preprint arXiv:1305.6497* **2013**.

[3] L. Wang, S. L. Jacques, L. Zheng, *Comput. Meth. Prog. Bio.* **1995**, 47, 131.

[4] T. L. Bergman, F. P. Incropera, D. P. DeWitt, A. S. Lavine, *Fundamentals of heat and mass transfer*, John Wiley & Sons, **2011**.

[5] a) P. Q. Jiang, X. Qian, R. G. Yang, L. Lindsay, *Phys. Rev. Mater.* **2018**, 2, 8; b) Y. Rah, Y. Jin, S. Kim, K. Yu, *Opt. Lett.* **2019**, 44, 3797; c) G. Cassabois, P. Valvin, B. Gil, *Nat. Photonics* **2016**, 10, 262.

[6] a) Z. Cheng, Y. R. Koh, A. Mamun, J. Shi, T. Bai, K. Huynh, L. Yates, Z. Liu, R. Li, E. Lee, M. E. Liao, Y. Wang, H. M. Yu, M. Kushimoto, T. Luo, M. S. Goorsky, P. E. Hopkins, H. Amano, A. Khan, S. Graham, *Phys. Rev. Mater.* **2020**, 4, 044602; b) R. i. database, Optical constants of AlN, https://refractiveindex.info/?shelf=main&book=AlN&page=Pastrnak-o, accessed: 2021; c) Aluminium nitride, https://en.wikipedia.org/wiki/Aluminium_nitride, accessed: 2021.

[7] a) H. Y. Chen, V. V. Ginzburg, J. Yang, Y. F. Yang, W. Liu, Y. Huang, L. B. Du, B. Chen, *Prog. Polym. Sci.* **2016**, 59, 41; b) Optical constants of BeO, https://refractiveindex.info/?shelf=main&book=BeO&page=Edwards-o, accessed: 2021; c) E. O. Wrasse, R. J. Baierle, in *15th Brazilian Workshop on Semiconductor Physics*, Vol. 28 (Eds: V. C. Anjos, S. O. Ferreira, H. W. L. Alves), Elsevier Science Bv, Amsterdam **2012**, p. 79.

[8] a) Optical constants of Si_3N_4, https://refractiveindex.info/?shelf=main&book=Si3N4&page=Luke, accessed: 2021; b) N. Manavizadeh, A. Khodayari, E. Asl-Soleimani, Springer Berlin Heidelberg, Berlin, Heidelberg 2009, 1120.

[9] a) Optical constants of SiC, https://refractiveindex.info/?shelf=main&book=SiC&page=Shaffer, accessed: 2021; b) Silicon carbide, https://en.wikipedia.org/wiki/Silicon_carbide, accessed: 2021.

[10] a) X. Wu, J. Lee, V. Varshney, J. L. Wohlwend, A. K. Roy, T. Luo, *Sci. Rep.* **2016**, 6, 22504; b) Optical constants of ZnO, https://refractiveindex.info/?shelf=main&book=ZnO&page=Bodurov, accessed: 2021; c) Zinc oxide, https://en.wikipedia.org/wiki/Titanium_dioxide, accessed: 2021.

[11] a) T. Gao, B. P. Jelle, *J. Phys. Chem. C* **2013**, 117, 1401; b) Optical constants of TiO_2, https://refractiveindex.info/?shelf=main&book=TiO2&page=Bodurov, accessed: 2021; c) Titanium dioxide, https://en.wikipedia.org/wiki/Titanium_dioxide, accessed: 2021.

[12] a) D. Lide, *CRC Handbook of Chemistry and Physics*, CRC Press, **2004**; b) Optical constants of ZrO_2, https://refractiveindex.info/?shelf=main&book=ZrO2&page=Bodurov, accessed: 2021; c) D. T. Jüstel, Physical Properties of Selected Optical Materials at Room Temperature (300 K), https://www.fh-muenster.de/ciw/downloads/personal/juestel/juestel/Bandgaps-Densities-IEPs-RefractiveIndices.pdf, accessed: 2021.

[13] a) Calcite, https://www.korth.de/index.php/162/items/11.html, accessed: 2021; b) Optical constants of $CaCO_3$, https://refractiveindex.info/?shelf=main&book=CaCO3&page=Ghosh-o, accessed: 2021.

[14] a) Thermal conductivity of $BaSO_4$, https://thermtest.com/materials-database, accessed: 2021; b) D. R. Lide, *CRC Handbook of Chemistry and Physics*, CRC Press, **2010**; c) A. M. Amiryan, A. M. Gurvieh, R. V. Katomina, I. Y. Petrova, N. P. Soshchin, M. I. Tombak, *J. Appl. Spectrosc.* **1977**, 27, 1159.

[15] a) Optical constants of Al_2O_3,

https://refractiveindex.info/?shelf=main&book=Al2O3&page=Malitson-o, accessed: 2021; b) R. C. R. Santos, E. Longhinotti, V. N. Freire, R. B. Reimberg, E. W. S. Caetano, *Chem. Phys. Lett.* **2015**, 637, 172.

[16] a) W. Zhu, G. Zheng, S. Cao, H. He, *Sci. Rep.* **2018**, 8, 10537; b) Optical constants of SiO_2, https://refractiveindex.info/?shelf=main&book=SiO2&page=Malitson, accessed: 2021; c) Silicon dioxide, https://en.wikipedia.org/wiki/Silicon_dioxide, accessed: 2021.

[17] a) Y. Nigara, *Jpn. J. Appl. Phys.* **1968**, 7, 404; b) P. H. Klein, W. J. Croft, *J. Appl. Phys.* **1967**, 38, 1603; c) W.-C. Wang, M. Badylevich, V. Afanas' ev, A. Stesmans, C. Adelmann, S. Van Elshocht, J. Kittl, M. Lukosius, C. Walczyk, C. Wenger, *Appl. Phys. Lett.* **2009**, 95, 132903.

[18] Optical constants of $(C_2H_6OSi)n$, https://refractiveindex.info/?shelf=organic&book=polydimethylsiloxane&page=Zhang-10-1, accessed: 2021.

[19] J. Mandal, Y. Yang, N. F. Yu, A. P. Raman, *Joule* **2020**, 4, 1350.

[20] J. Mandal, Y. Fu, A. C. Overvig, M. Jia, K. Sun, N. N. Shi, H. Zhou, X. Xiao, N. Yu, Y. Yang, *Science* **2018**, 362, 315.

[21] H. Zhang, K. C. S. Ly, X. Liu, Z. Chen, M. Yan, Z. Wu, X. Wang, Y. Zheng, H. Zhou, T. Fan, *Proc. Natl. Acad. Sci. U. S. A.* **2020**, 117, 14657.

[22] T. Li, Y. Zhai, S. He, W. Gan, Z. Wei, M. Heidarinejad, D. Dalgo, R. Mi, X. Zhao, J. Song, J. Dai, C. Chen, A. Aili, A. Vellore, A. Martini, R. Yang, J. Srebric, X. Yin, L. Hu, *Science* **2019**, 364, 760.